Wave damping of a sloshing wave by an interacting turbulent vortex flow

Francisco Reyes [ORCID],[1] Vicente Torrejón [ORCID],[1] and Claudio Falcón[1,2,*]

[1]*Departamento de Física, Facultad de Ciencias Físicas y Matemáticas, Universidad de Chile, Casilla 487-3, Santiago, Chile*
[2]*Millenium Nucleus of Soft Smart Mechanical Metamaterials, Santiago, Chile*

We report on the enhancement of the hydrodynamic damping of gravity waves at the surface of a fluid layer as they interact with a turbulent vortex flow in a sloshing experiment. Gravity surface waves are excited by oscillating horizontally a square container holding our working fluid (water). At the bottom of the container, four impellers in a quadrupole configuration generate a vortex array at moderate to high Reynolds number, which interact with the wave. We measure the surface fluctuations using different optical nonintrusive methods and the local velocity of the flow. In our experimental range, we show that as we increase the angular velocity of the impellers, the gravity wave amplitude decreases without changing the oscillation frequency or generating transverse modes. This wave dissipation enhancement is contrasted with the increase of the turbulent velocity fluctuations from particle image velocimetry measurements via a turbulent viscosity. To rationalize the damping enhancement a periodically forced shallow water model including viscous terms is presented, which is used to calculate the sloshing wave resonance curve. The enhanced viscous dissipation coefficient is found to scale linearly with the measured turbulent viscosity. Hence, the proposed scheme is a good candidate as an active surface gravity wave dampener via vortex flow reconfiguration.

I. INTRODUCTION

When a partially filled liquid container is moved or pushed, the fluid inside is displaced. As this happens, its free surface oscillates displaying waves. These waves interact strongly with the container, changing the motion of both the wave and the container. This is known as sloshing [1]. The sloshing of the fluid layer can attain very large amplitudes which may produce spilling of the inner fluid or destabilization of the container. One deals with this problem daily (and rather unconsciously) when trying to walk with the morning cup of tea or coffee without spilling it [2]. This simple problem, however, has vast implications in the transport and containment of large amounts of liquid fuel, on the movement and displacements of ships and vessels, and on the motion and dynamics of large fluid masses in dams and lakes [1]. Consequently, intense investigations on the parameters determining the generation, evolution, and dynamics of liquid sloshing in containers of different shapes and sizes have been carried out since the end of the 19th century [3].

To avoid violent changes in the liquid height near the containers walls which induces destabilization and spillovers, several schemes are proposed to reduce the liquid motion. These schemes are usually based on changing the container geometry or the boundary conditions of the wave at its wall (see Ref. [1] and references therein). Active control can also be applied, which can be triggered by the current state of the wave height [4,5]. Here we explore how fluid motion itself may provide an alternative control mechanism for sloshing. Specifically, we study how a vortex flow attenuates low-frequency resonances of surface gravity waves within a container. The attenuation of surface waves by vortical fluid motion has been intensively considered in physics and oceanography [6–12]. In these studies the wave-vortex interaction enhances the surface wave damping via strong nonlinear interactions (especially in the case of hydrodynamic turbulence at large Reynolds numbers). Thus, these configurations generate higher order modes (or in the case of Refs. [13,14], subharmonic behavior) that are coupled to the main wave and are thus hard to disentangle. In order to understand the damping enhancement via wave-vortex interaction in a simpler setup is needed.

Here we present an experimental study on the damping of a sloshing wave developing in a sinusoidally forced container as it interacts with a vortex flow at moderate to high Reynolds number. We characterize the response of the wave by computing its experimental resonance curve as a function of the forcing frequency. As we increase the vortex flow angular frequency this resonance curve flattens, which is understood as an enhancement of the sloshing wave's damping coefficient in a long-wavelength approximation. A viscous shallow water set of equations is proposed which allows us to calculate the resonance curve in the linear regime. We relate the damping enhancement of the long sloshing wave to the small-scale turbulent fluctuations by computing an average turbulent viscosity and comparing it to the measured damping coefficient extracted from the wave's resonance curve. These two coefficients, one measured from the resonance curve of a long sloshing wave while the other is measured from the internal small-scale turbulence, are found to be proportional. Thus, this wave-vortex interaction scheme looks like a good candidate for active damping enhancement for liquid containers.
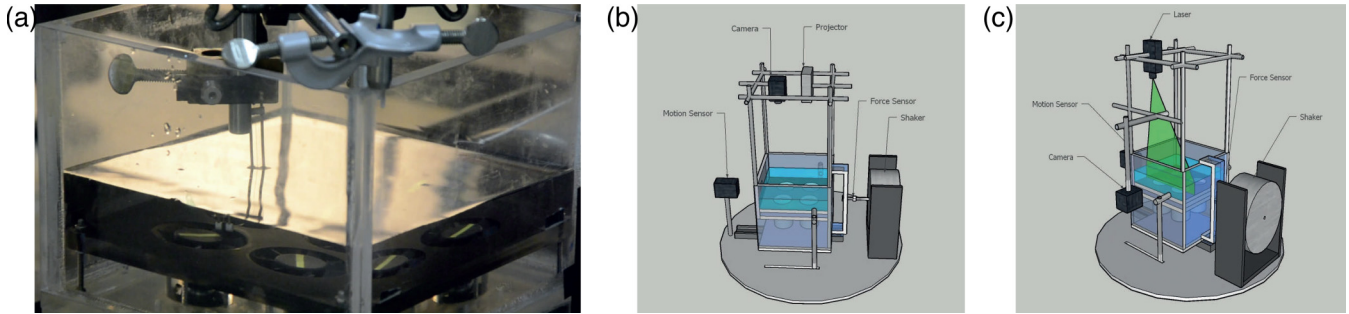
*cfalcon@ing.uchile.cl

FIG. 1. (a) Experimental setup displaying a sloshing wave. At the bottom of the cell one can observe the fake bottom including four impellers. (b) Experimental setup scheme including the FTP scheme mounted on top of the experimental cell. (c) Experimental setup including the edge-detection scheme used for both one-dimensional detection and PIV measurements.

The paper is divided as follows. In Sec. II we describe our experimental setup, the flow configuration we used, and its nondimensional numbers. In Sec. III we detail the techniques used to track surface and velocity fluctuations and the analysis we used to study their dependence on f_m. In Sec. IV we propose an heuristic modification of shallow water set of equations including viscosity, which we use to relate both the measured wave damping with the small-scale velocity fluctuations. Finally, in Sec. V we conclude and discuss possible ramifications of our work.

II. EXPERIMENTAL SETUP

The experimental setup is depicted in Fig. 1. It is composed of a plexiglass container of volume $19.0 \times 19.0 \times 11.0$ cm^3 which is filled with distilled water (density $\rho = 1000$ kg/m^3, kinematic viscosity $\nu_o = 10^{-6}$ m^2/s) up to a height $h_o = 3$ cm. Full surface contamination of the air-water interface is achieved, as we perform our experiments after 1 hr of pouring the fluid within the container. Four small motors are placed at the bottom of the container in a square array. The rotation axis of each one is located 7 cm away from the closest wall of container. Attached to each motor axis is an impeller with a diameter $a = 6$ cm. A horizontal plate covers the area without impellers and acts as the effective bottom of the experimental cell. Each motor is driven by an independent dc power supply and can turn at a frequency $f_m \in [0, 3.5]$ Hz in a chosen direction, generating a vortex flow. The angular velocity of each motor is measured independently as a function of their driving voltage. The magnitude of f_m for each motor is the same, but the sign changes forming a quadrupole, as depicted in Fig. 1. We have chosen this arrangement because, while it presents a very strong shear flow, it displays no large-scale mean flow (which can be coupled to the wave creating transverse motion). The flow has a large-scale Reynolds number Re $= 2\pi f_m a^2/\nu \in [3000, 20000]$ and Froude number Fr $= 4\pi^2 f_m^2 a^2/gh_o < 1.5$. At these moderate to high Re values, the flow is turbulent and will become important for the motion and damping of surface waves. It must be noticed that for Fr > 1 ($f_m < 3$ Hz) we observe surface deformations over the center of each impeller of the order of the wave amplitude at that position, and thus for these values of f_m a non-negligible coupling between wave and vortex-induced surface fluctuations may develop. The possibility of surface deformations by the flow is also supported by the fact that the Webber

number We $= 4\pi^2 f_m^2 a^3 \rho/\gamma > 1$, where $\gamma \simeq 70$ mN/m is the water-air surface tension coefficient.

The container, including the four motors, is mounted on a rail allowing the unidirectional motion of the whole setup. This motion is enforced by to optical posts acting as secondary guides for the motion of the container. Along the rail, a horizontal sinusoidal forcing with frequency $f \in [1.35, 1.75]$ Hz (angular frequency $\omega = 2\pi f$) is imposed using an electromagnetic shaker driven by a power amplifier controlled by a personal computer. The motion of the container is monitored in the same direction of the forcing using a laser displacement sensor, which delivers a signal $X(t)$. The signal is then digitalized at 1 kHz using an acquisition card via LabView and filtered digitally at f with a 1 Hz bandwidth. Applying a sinusoidal driving does not imply that the system will respond sinusoidally as higher harmonics may develop. We have checked that higher order harmonics of $X(t)$ are two to three orders of magnitude smaller than the fundamental harmonic oscillating at f. Typical acquisitions times (for fixed experimental parameters) last between 30 up to 60 sec, although test measurements were acquired for 1 or 2 hr. In our experimental setup X_o, h_o, f_m, and f are the control parameters. Typical amplitudes of the generated surface waves $\delta\eta \in [0.1, 0.3]$ cm set our experiments in the limit of small steepness $\delta\eta/h_o \in [0.03, 0.13]$ and Ursell numbers $\delta\eta/k^2 h_o^3 \in [0.01, 0.40]$. In these limits, linear wave theory for surface waves is applicable [1], which simplifies the understanding of the problem. In this linear regime, surface deformations with the largest available wavelength ($\lambda^* = 38$ cm) develop in the same (longitudinal) direction of the forcing with no transverse oscillations. Thus, for $h_o = 3$ cm, the theoretically computed oscillation frequency of surface gravity waves in the long wavelength limit $\lambda \gg h_o$ is $f^* = \sqrt{gh_o}/\lambda^* \simeq 1.43$ Hz.

III. MEASUREMENT TECHNIQUES AND RESULTS

We explore the wave-vortex structure in this configuration by mounting onto the container two different image acquisition schemes. First, we mount a Fourier transform perfilometry (FTP) scheme [15] allowing us to access the spatiotemporal surface fluctuations $\eta(x, y, t)$, with (x, y) spanning the area of the container. Titanium oxide in its anatase phase from Kronos (Kronos 1002) is added to our working fluid in a concentration of 4 g/l, making the air-water interface strongly diffusive to light without changing radically the fluid's
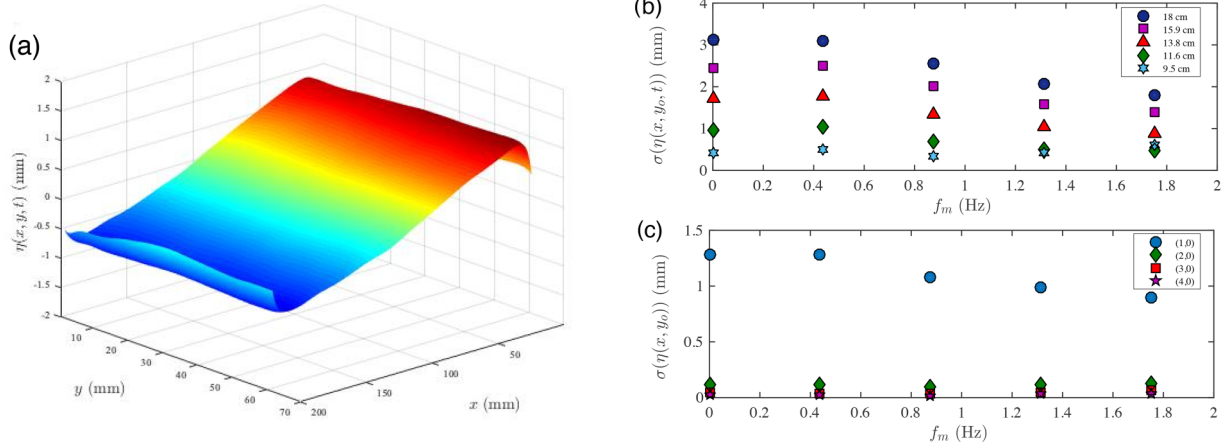
FIG. 2. (a) Typical FTP data for $f = 1.45$ Hz, $X_o = 0.02$ cm, and $f_m = 0$ Hz. (b) rms fluctuations $\sigma(\eta(x, y_o, t))$ at $f = 1.45$ Hz as a function of f_m for $x = 18.0$ (○), 15.9 (□), 13.8 (△), 11.6 (◇), and 9.5 (∗) cm from one wall. (c) rms fluctuations $\sigma_{n,m}$ at $f = 1.45$ Hz as a function of f_m for the (1,0) 18.0 (○), (2,0) (◇), (3,0) (□), and (4,0) (⋆) modes.

rheological properties [16]. A 10-bit CCD camera and a microprojector, separated by $D = 5$ cm, were positioned at a height $H = 45$ cm of the fluid-free surface. The spatial resolution in both directions is the size of the projected pixel (0.015 cm). Spatially, the wavelength of the projected fringes is set at 0.5 cm, much smaller than the typical spatial scales of both the vortex and wave fields. Temporally, the acquisition frequency is set at 20 Hz, which is much larger than f_m and f, allowing the observation of both wave and vortex temporal scales, while the acquisition time was set at 25 s. The interrogation window is half the surface area of the box (9.5×19.0 cm^2). To compute the surface fluctuations we use the symmetry of the surface normal modes, avoiding large speckle reflections of the projected light on the unused other half of the box's surface area. Second, we mount an edge detection scheme [17] to track the air-water interface along a line which also serves also as a particle image velocimetry (PIV) scheme, allowing us to access the spatiotemporal surface fluctuations $\eta(x, y_o t)$ at a given distance y_o of a container wall, and the two-dimensional velocity field underneath $\eta(x, y_o, t)$. Fluorescein from M&B is added to our working fluid in a concentration of 4 mg/l in order to enhance illumination contrast at the interface. We also added 100 μm silver-coated hollow glass spheres from Dantec Dynamics to the fluid in a concentration of 0.1 mg/l, which are used to compute the velocity field of within the fluid. In this configuration, the camera is mounted facing one of the transparent walls of the container in a shallow angle ($<5°$) to avoid confusion with the meniscus. In the case of edge detection measurements, the acquisition frequency is set at 20 Hz with an interrogation window of 9.5×19.0 cm^2 with a 0.05 cm/pix sensitivity allowing the detection of the entire surface deformations along the container. In the case of PIV measurements, the acquisition frequency is set at 100 Hz with an interrogation window of 9.5×3.0 cm^2 with a 0.02 cm/pix sensitivity centered over an impeller. These schemes are depicted in Fig. 1.

Using the FTP data, we can quantify the effect of the vortex flow on the wave structure and its modal content by tracking the local surface fluctuations at different points on the

experimental cell. For this, we set $f = f^*$ and $X_o = 0.02$ cm. A typical image of the surface profile is shown in Fig. 2(a). From the acquired data we measure locally the surface profile $\eta(x, y_o, t)$ along a line that passes through the center of the cell in the longitudinal (x) direction towards one of the walls at a fixed transverse position ($y = y_o = 9$ cm). We find that the surface rms fluctuations at each position decrease as we increase f_m in Fig. 2(b). This behavior is independent of the chosen position in the transverse (y) direction. For this mode, when $f_m = 0$ the peak amplitude of the surface fluctuations near the wall is almost 2 times larger when compared to the $f_m = 1.75$ Hz case.

To further understand how the vortex flow changes the modal structure of the wave, we decompose the surface fluctuations into normal modes as

$$\eta(x, y, t) = \sum_{n,m=0}^{N,M} A_{n,m}(t) \cos(k_n x) \cos(k_m y), \quad (1)$$

with $(k_n, k_m) = (2\pi/L) \times (n, m)$ using $L = 19$ cm and $\omega^* = 2\pi f^*$. Here the normal modes of the linear surface gravity wave problem are cosine functions of the longitudinal (x) and transverse (y) coordinates, which satisfy the zero normal velocity boundary conditions at the container's walls [18]. We numerically compute the projection of $\eta(x, y, t)$ onto the different modes, $A_{n,m}(t)$, for every time step (set by the acquisition frequency of the FTP scheme) for $n = 1, \ldots, N$ and $m = 1, \ldots, M$. From this temporal trace we compute the rms fluctuations of $A_{n,m}(t)$, $\sigma_{n,m}$, for different values of (n, m) as a function of f_m, as is depicted in Fig. 2. In this projection, care is taken to avoid the border of the cell where the meniscus causes speckles and light spots of high intensity that create spurious data points in $\eta(x, y, t)$. We choose, for this experimental configuration, $N = M = 4$. Larger values of N and M generate amplitudes that are at least three orders of magnitude smaller than the one for the fundamental mode $(n, m) = (1, 0)$. To avoid speckle and illumination problems we use the symmetry of the modes with respect to the center line of the cell to simplify the mode projection calculation. For $f^* = 1.43$ Hz, the sloshing mode rms fluctuations $\sigma_{1,0}$
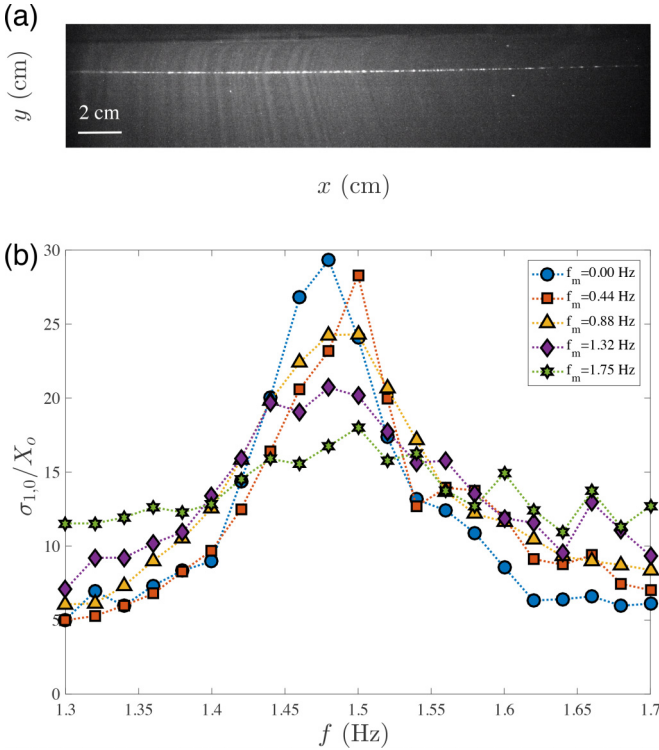
(a)

(b)

FIG. 3. (Top) Typical image of the surface wave. The white line in the middle of the image depicts the air-water interface. (Bottom) Normalized surface wave fluctuations $\sigma_{1,0}/X_o$ as a function of f for $f_m = 0.00$ (○), 0.44 (□), 0.88 (△), 1.32 (◇), and 1.75 (∗) Hz.

decreases as f_m increases, following the behavior observed above. In this case $\sigma_{1,0}$ decreases up to 30% when f_m is increased up to 1.75 Hz. The rms fluctuations of the other modes, including the sloshing modes harmonics, are two orders of magnitude smaller and do not increase their amplitude with increasing f_m as much as the sloshing mode rms fluctuations decrease [cf. Fig. 2(c)]. Thus, for our experimental configuration, the wave-vortex interaction increases the wave damping of the gravest mode without contributing strongly to the development of higher order modes. It must be stressed that nonlinear wave-vortex interaction is always present, but from the observed wave dynamics in our experiment its effect on harmonic generation can be neglected.

With this in mind, we study the longitudinal sloshing mode dependence on f and f_m using the simple edge detection scheme described above. Typical images of the surface deformation, including its detected edge, are shown in Fig. 3. We fix $y = y_o$ at a distance of 3 cm from closest wall to the camera. The amplitude of the surface wave $A_{1,0}$ is computed by projecting the detected edge onto the gravest surface normal mode, as explained above. As we vary $f \in [1.3, 1.7]$ Hz with a frequency step $\Delta f = 0.02$ Hz and fix $f_m = 0$ Hz, the amplitude of the surface wave follows a well-known resonance curve. It increases its value with f to reach a maximum at $f = 1.47$ Hz, which is less than 3% smaller than f^* to then decrease as f increases. The normalized surface wave rms fluctuations $\sigma_{1,0}/X_o$ are shown in Fig. 3 as a function of f. When $f_m \neq 0$, the curve changes quantitatively: increasing f_m decreases the curve's maximum value while increasing its
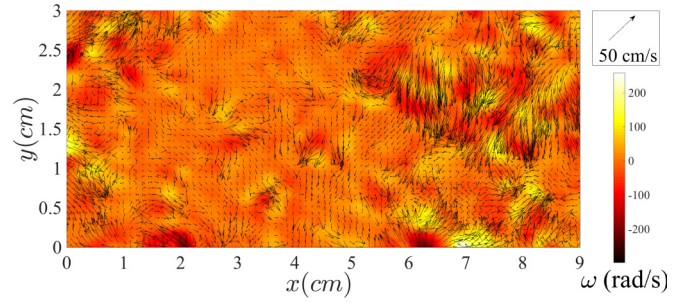

FIG. 4. Instantaneous velocity field (arrows) and vorticity (color map) for $f_m = 0.44$ Hz at f^*. Typical velocity scale is depicted on the upper corner.

width, showing the enhanced damping of the system. A very slight shift of f^* is also observed towards larger frequencies, as f_m is increased.

We turn to the study of the two-dimensional velocity field within the layer to understand the observed damping enhancement due to the effect of the impellers. With the experimental measurement scheme presented before, we compute $\mathbf{u}(x, y_o, z, t)$ using PIVLab [16] in Matlab. We reduce the interrogation window, neglecting the free surface deformations measured from the flat state. To track high-amplitude velocity fluctuations we increase the acquisition frequency up to 100 Hz. We divide $\mathbf{u}(x, y_o, z, t)$ in two time-filtered components $\mathbf{u} = \mathbf{U} + \delta\mathbf{u}$, where $\mathbf{U}$ is a low-pass filtered component at twice the forcing frequency and $\delta\mathbf{u}$ is the high-frequency (turbulent) component. For every point in space, $\mathbf{U}$ presents a dominant oscillation frequency (which is set by f^*), while slower motions also appear as f_m increases. In the case of $\delta\mathbf{u}$, high-frequency (turbulent) fluctuations developed with larger and larger amplitude as f_m increases. We focus on tracking $\delta\mathbf{u}$ and its in-plane vorticity $\Omega = (\nabla \times \delta\mathbf{u}) \cdot \hat{j}$, with $\hat{j}$ the unit vector normal to the x-z plane. In Fig. 4 we depict an instantaneous snapshot of $\delta\mathbf{u}$ and Ω. As we increase f_m, smaller patches of velocity fluctuations appear in shorter bursts which fill the entire shallow water layer. A similar behavior is also observed for the in-plane vorticity. From the local fields described above, we compute the global rms turbulent velocity fluctuations $\delta\bar{u}$ and vorticity $\bar{\Omega}$ by averaging the local rms fluctuations of each field on every position in space in each image and then averaging along all images. We observe that $\delta\bar{u}$ increases monotonically with f_m while $\bar{\Omega}$ remains roughly constant.

IV. THEORETICAL MODELING

We rationalize these experimental observations in the shallow water limit including viscosity [19–22] which we will use to relate the large-scale wave damping of the sloshing wave with the measured small-scale velocity fluctuations of the shearing flow generated by the impellers. It must be stressed that this is a heuristic approach to the problem at hand, and that the predictions it makes will serve as an *ad hoc* relation between the dynamics of large and small scales in our problem. We assume that the container is a square box of lateral side L and depth h_o. The coupled equations for the local

height $h(x, y, t) = h_o + \eta(x, y, t)$ and depth-averaged velocity field $\mathbf{u}(x, y, t)$ are [20–22]

$$\partial_t h + \nabla \cdot (h\mathbf{u}) = 0, \qquad (2)$$

$$\partial_t \mathbf{u} + \mathbf{u} \cdot \nabla \mathbf{u} + g\nabla h = +h^{-1}\nabla \cdot [h\nu_o(\nabla \mathbf{u} + \nabla \mathbf{u}^T)$$
$$- h\nu_o(\nabla \cdot \mathbf{u})] - \alpha_o \mathbf{u} + \ddot{X}(t)\hat{x}, \qquad (3)$$

with $\nabla = (\partial_x, \partial_y)$. Here we have included the first-order corrections on viscosity, condensed on a depth-averaged viscous stress tensor (third line), and a the shallow water friction coefficient α_o (which depends on the fluid's kinematic viscosity ν_o, the wave spatiotemporal scales, and the nature and structure of the underlying flow). We have added a forcing term $\ddot{X}(t)$ which comes from the local horizontal acceleration of the fluid's container in the $\hat{x}$ direction. In the linear regime, Eqs. (4) can be rewritten for the longitudinal component of the velocity field u_x as

$$\partial_{tt} u_x + \alpha_o \partial_t u_x - \nu \partial_{xx}\partial_t u_x - gh_o \partial_{xx} u_x = \ddot{X}(t). \qquad (4)$$

As the fluid container moves along the $\hat{x}$ direction following the prescription $X(t) = \text{Re}(X_o e^{i\omega t})$, we assume that the velocity field and surface deformation perturbations describing the gravest sloshing wave of the container can be written as $\mathbf{u}(x, y, t) = u_x(x, t)\hat{x} \sim \text{Re}(u_o e^{i(kx - \omega t)})\hat{x}$ and $\eta(x, t) \sim \text{Re}(\eta_o e^{i(kx - \omega t)})$, respectively. Here $k = 4\pi/L$ is the wave vector of the sloshing wave [mode (1,0)]. For u_o, the above equation can be reduced to a simple linear equation

$$u_o = \left[\frac{-i\omega^3}{\omega^2 - \omega_o(k)^2 - i(\alpha_o + \nu k^2)\omega} \right] X_o, \qquad (5)$$

where we have used the inviscid shallow water dispersion relation $\omega_o(k) = (gh_o)^{1/2}k$. With this result, we can compute the normalized wave amplitude

$$\left| \frac{\eta_o}{X_o} \right| = \frac{kh_o\omega^2}{\sqrt{[\omega^2 - \omega_o(k)^2]^2 + (\alpha_o + \nu k^2)^2\omega^2}}. \qquad (6)$$

As the container moves sinusoidally, we estimate Stokes boundary layer $\Delta \sim \sqrt{\nu_o/\omega} \ll h_o \ll L$. Thus, from the ratio of the flow's kinetic energy to the dissipated power within Δ, we estimate a typical damping rate, at the large scale using our experimental parameters as $\alpha_o \sim \nu_o/(\Delta h_o) = 0.1 \text{ s}^{-1}$. It is important to notice that with these values, the estimated maximum value of the resonance curve at $f_m = 0$ Hz from Eq. (6) is $|\eta_o/X_o| \sim 30$, which is of the same order of magnitude of the measured value from Fig. 3. Also as $\alpha_o/(\nu_o k^2) \sim 400$, we will neglect, in what follows the viscous effect of the momentum diffusion term νk^2 on the resonance curve from Fig. 4.

Using the resonance curve from above and the velocity field acquired above from from PIV measurements, we intend to quantify the effect of the small-scale turbulent velocity field on the sloshing wave damping using Eqs. (4). As we observed before, the width of the resonance curve increases with f_m while the resonance frequency f^* moves very slightly to the higher values (less than 5%). Similarly, the turbulent fluctuations rms also increase with f_m. In order to relate these observations, we will model the large-scale damping rate as a function of the turbulent velocity. Thus, we change α_o to α in Eq. (6) to fit the curve's width as a function of f_m following
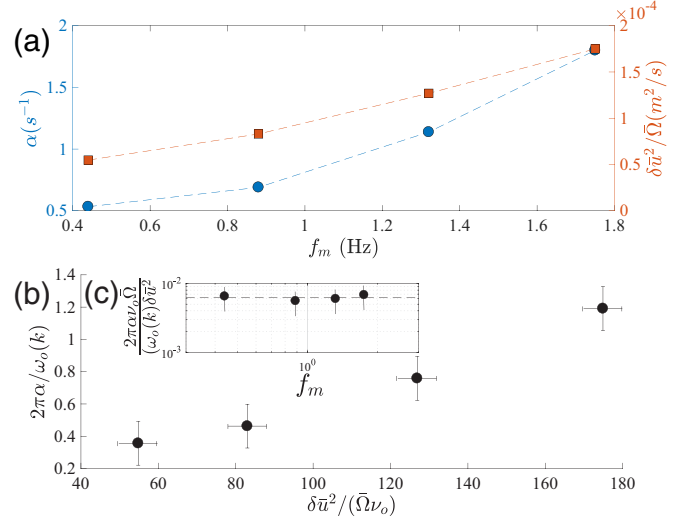

FIG. 5. (a) α (left axis) and $\delta\bar{u}^2/\bar{\Omega}$ (right axis) as a function of f_m. (b) Normalized damping parameter per wave period $2\pi\alpha/\omega_o(k)$ as function of the normalized turbulent viscosity $\delta\bar{u}^2/(\bar{\Omega}\nu_o)$. Inset: $(2\pi\alpha\nu_o\bar{\Omega})/[\omega_o(k)\delta\bar{u}^2]$ as a function of f_m.

the proposed arguments found in Ref. [11]. It must be noticed that when $f_m = 0$, we calculate $\alpha_o \sim 0.4 \text{ s}^{-1}$, which is of the same order of magnitude as the one estimated above. We will assume that α is a function of the rms turbulent fluctuations which are averaged at the integral scale (the container's side). This is the same scale of the sloshing wave. In that sense, it is reasonable to compute an effective large-scale parameter stemming from the underlying turbulent small scales. We quantify this effect on the large-scale sloshing wave via a turbulent (Boussinesq) viscosity coefficient $\nu_T = \beta \times \delta\bar{u} \times l$, where l is the Taylor microscale of the system, which we compute as $l = \delta\bar{u}/\bar{\Omega}$ [23]. Note that $\delta\bar{u}^2/(\bar{\Omega}\nu_o)$ is the Reynolds number estimated at Taylor's microscale Re_λ. Here β is a fitting parameter of order one which depends on the structure of the flow [23]. In Fig. 5(a) we plot both α and $\delta\bar{u}^2/\bar{\Omega}$ as a function of f_m which shows their monotonic growth. To further understand this trend we plot α as a function of $\delta\bar{u}^2/\bar{\Omega}$. We normalize both variables, so α is divided by the sloshing wave frequency $f^* = \omega_o(k)/(2\pi)$ and $\delta\bar{u}^2/\bar{\Omega}$ by the fluid's viscosity ν_o. Error bars come from the 95% confidence interval for α and from the standard deviation of $\delta\bar{u}^2/\bar{\Omega}$. We plot the dependence of $2\pi\alpha/\omega_o(k)$ as function of $\delta\bar{u}^2/(\bar{\Omega}\nu_o)$ in Fig. 5(b). We observe a roughly linear dependence of α on $\delta\bar{u}^2/\bar{\Omega}$ and thus on ν_T. To wit, we also plot the ratio of these quantities as we increase f_m in the inset of Fig. 5(b), which remains roughly constant at 6.5×10^{-3}. Although there are large fluctuations on the observed values, they show clearly that we can quantify the damping coefficient as a function of the global rms fluctuations generated by the impellers via a large-scale turbulent (eddy) drag coefficient in the shallow water limit.

V. CONCLUSIONS

In conclusion, we show the enhancement of the hydrodynamic damping of gravity waves at the surface of a shallow fluid layer as they interact with a vortex quadrupole in a

sloshing experiment generated by an array of impellers. In our experimental limit, as we increase the angular velocity of the impellers $2\pi f_m$, the surface gravity wave amplitude decreases its amplitude without changing the oscillation frequency or generating new modes, which is quantified using an two-dimensional optical profilometry technique. In the case of the sloshing (gravest) mode its amplitude decreases in half when f_m is increase from 0 to 1.75 Hz. We quantify this damping enhancement via the change on the resonance curve of the sloshing wave, measured by an optical edge detection technique. The resonance curve becomes wider as the effective wave damping α increases. We couple this observation with PIV measurements, which allows us to quantify the local and global turbulent rms fluctuations and their respective vorticity fluctuations. From these quantities, we compute an effective turbulent viscosity ν_T which is shown to be proportional to α. Thus we can rationalize and quantify the damping enhancement of the large-scale sloshing wave by small-scale (with respect to the sloshing wave) turbulent fluctuations using a turbulent viscosity coefficient. This damping scheme can be adapted to actively attenuate surface gravity waves or to actively change the vortex flow configurations, which may served to control the wave damping and thus the wave amplitude of the sloshing wave.

[1] R. A. Ibrahim, *Liquid Sloshing Dynamics: Theory and Applications* (Cambridge University Press, Cambridge, 2005).

[2] H. Mayer and R. Krechetnikov, Walking with coffee: Why does it spill?, Phys. Rev. E **85**, 046117 (2012).

[3] S. S. Hough, XII. The oscillations of a rotating ellipsoidal shell containing fluid, Philos. Trans. R. Soc. London A **186**, 469 (1895).

[4] J. G. Anderson, S. E. Semercigil, and Ö. F. Turan, A standing-wave-type sloshing absorber to control transient oscillations, J. Sound Vib. **232**, 839 (2000).

[5] K. I. Yano and K. Terashima, Robust liquid container transfer control for complete sloshing suppression, IEEE Trans. Control Syst. Technol. **9**, 483 (2001).

[6] O. M. Phillips, The scattering of gravity waves by turbulence, J. Fluid Mech. **5**, 177 (1959).

[7] H. S. Olmez and J. H. Milgram, An experimental study of attenuation of short water waves by turbulence, J. Fluid Mech. **239**, 133 (1992).

[8] R. Savelsbergand and W. van de Water, Experiments on free-surface turbulence, J. Fluid Mech. **619**, 95 (2009).

[9] O. Bühler, Wave-vortex interactions in fluids and superfluids, Annu. Rev. Fluid Mech. **42**, 205 (2010).

[10] P. Gutiérrez and S. Aumaître, Surface waves propagating on a turbulent flow, Phys. Fluids **28**, 025107 (2016).

[11] T. Green, H. Medwin, and J. E. Paquin, Measurements of surface wave decay due to underwater turbulence, Natl. Phys. Sci. **237**, 115 (1972).

[12] A. G. Boyev, The damping of surface waves by intense turbulence, Izv. Atmos. Ocean Phys. **7**, 31 (1971).

[13] C. Falcón and S. Fauve, Wave-vortex interaction, Phys. Rev. E **80**, 056213 (2009).

[14] S. A. Ermakov, I. A. Kapustin, and O. V. Shomina, Laboratory investigation of damping of gravity-capillary waves on the surface of turbulized liquid, Izv. Atmos. Ocean Phys. **50**, 204 (2014).

[15] A. Maurel, P. Cobelli, V. Pagneux, and P. Petitjeans, Experimental and theoretical inspection of the phase-to-height relation in Fourier Transform Profilometry, J. Appl. Opt. **48**, 380 (2009); P. Cobelli, A. Maurel, V. Pagneux, and P. Petitjeans, Global measurement of water waves by Fourier Transform Profilometry, Exp. Fluids **46**, 1037 (2009).

[16] W. Thielicke and E. J. Stamhuis, PIVlab—Towards user-friendly, affordable and accurate digital particle image velocimetry in MATLAB, J. Open Res. Softw. **2**, e30 (2014).

[17] S. Nazarenko, S. Lukaschuk, S. McLelland, and P. Denissenko, Statistics of surface gravity wave turbulence in the space and time domains, J. Fluid Mech. **642**, 395 (2010).

[18] L. D. Landau and E. M. Lifshitz, *Course of Theoretical Physics*, Vol. 2 (Pergamon, New York, 1959).

[19] J. N. Hunt, The viscous damping of gravity waves in shallow water, Houille Blanche **18**, 685 (1964).

[20] C. D. Levermore and M. Sammartino, A shallow water model with eddy viscosity for basins with varying bottom topography, Nonlinearity **14**, 1493 (2001).

[21] D. Bresch and B. Desjardins, Existence of global weak solutions for a 2D viscous shallow water equations and convergence to the quasi-geostrophic, Model. Comm. Math. Phys. **238**, 211 (2003).

[22] F. Marche, Derivation of a new two-dimensional viscous shallow water model with varying topography, bottom friction and capillary effects, Eur. J. Mech. B **26**, 49 (2007).

[23] S. B. Pope, *Turbulent Flows* (Cambridge University Press, Cambridge, 2000).